Clustering of Red Galaxies around the Z = 1.53 Quasar 3C 270.1

Share Your Story

The Harvard community has made this article openly available.
Please share how this access benefits you. Submit a story .

Accessibility

CLUSTERING OF RED GALAXIES AROUND THE $z = 1.53$ QUASAR 3C 270.1

Martin Haas[1], S. P. Willner[2,5], Frank Heymann[1,3], M. L. N. Ashby[2,5], G. G. Fazio[2], Belinda J. Wilkes[2], Rolf Chini[1], Ralf Siebenmorgen[3], and Daniel Stern[4]

[1] Astronomisches Institut, Ruhr-Universität Bochum, Universitätsstraße 150, 44801 Bochum, Germany; haas@astro.rub.de
[2] Harvard-Smithsonian Center for Astrophysics, 60 Garden Street, Cambridge, MA 02138, USA
[3] European Southern Observatory, Karl-Schwarzschildstr. 2, 85748 Garching, Germany
[4] Jet Propulsion Laboratory, California Institute of Technology, Pasadena, CA 91109, USA

ABSTRACT

In the paradigm of hierarchical galaxy formation, luminous radio galaxies mark mass assembly peaks that should contain clusters of galaxies. Observations of the $z = 1.53$ quasar 3C 270.1 with the *Spitzer Space Telescope* at 3.6–24 μm and with the 6.5 m MMT in the z' and Y bands allow the detection of potential cluster members via photometric redshifts. Compared with nearby control fields, there is an excess of ∼11 extremely red objects (EROs) at $1.33 \leqslant z_{\rm phot} \leqslant 1.73$, consistent with a protocluster around the quasar. The spectral energy distributions of 3/4 of the EROs are better fitted with passive elliptical galaxies than with dust-reddened starbursts, and of four sources well detected on an archival *Hubble Space Telescope* (*HST*) snapshot image, all have undisturbed morphologies. However, one ERO, not covered by the *HST* image, is a double source with 0″.8 separation on the z' image and a marginal (2σ) 24 μm detection indicating a dust-enshrouded starburst. The EROs are more luminous than $L^{\star}$ ($H = -23.6$ AB mag at $z \approx 1.5$).

Key words: galaxies: clusters: individual (3C270.1) – infrared: galaxies – quasars: general

1. INTRODUCTION

Groups and clusters of galaxies are key targets for studying the evolution of galaxies and large-scale structures. In the local universe thousands of clusters are known, but at high redshift ($z > 1$) only few clusters have been identified due to the challenge of discriminating a distant cluster from the abundant foreground galaxies.

A few high-redshift clusters have been found via X-ray observations of a hot intracluster medium (ICM) up to $z = 1.45$ (Mullis et al. 2005; Bremer et al. 2006; Stanford et al. 2006; Fang et al. 2007). Clusters up to this redshift range have also been found by searching for galaxy overdensities in wide-area optical-infrared surveys, for instance, the *Spitzer*-IRAC shallow survey (Stanford et al. 2005; Eisenhardt et al. 2008), the UKIDSS ultra-deep survey (van Breukelen et al. 2006), HIROCS/COSMOS (Zatloukal et al. 2007), and the *Spitzer* First Look Survey (Muzzin et al. 2008).

An alternative way to find high-redshift clusters is to use radio sources as signposts. Luminous radio sources occur in massive galaxies ($>10^{11} M_{\odot}$; Seymour et al. 2007), which according to the hierarchical formation model represent mass assembly peaks of the early universe. As such, they are expected to trace overdense regions and therefore cluster formation sites. The invaluable advantage of searching for clusters around radio sources is that one knows the redshift to search and therefore one can limit the observational effort.

Searches around very high redshift ($2 < z < 5$) radio sources have found an excess of Lyman α-emitting galaxies (Kurk et al. 2000; Miley et al. 2004; Venemans et al. 2007). These protoclusters show a rather large projected extent and only a loose concentration, consistent with clusters that are forming but not yet virialized (Intema et al. 2006; Zirm et al. 2008).

Based on small ($<2'$) maps, tentative (2σ–3σ) evidence for an overdensity of extremely red objects (EROs; $R - K > 5$) around

high-redshift ($1 < z < 3$) radio sources has been reported (Best 2000; Sánchez & González-Serrano 2002; Stern et al. 2003; Toft et al. 2003; Wold et al. 2003; Zirm et al. 2008). These EROs could be high-redshift passive ellipticals or dust-reddened star-forming galaxies. This ambiguity leaves open the question of whether the giant ellipticals were already in place at these redshifts, implying a formation redshift larger still, or whether the EROs are starbursts and we are probing the epoch at which the cluster ellipticals formed.

Using the *Spitzer Space Telescope* (*SST*; Werner et al. 2004), we are performing a 3.6–24 μm survey of the complete 3CR sample of radio galaxies and quasars at $1 < z < 2.5$ (Haas et al. 2008). The large ($>5'$) *Spitzer* arrays enable us to explore also the environment of the high-redshift radio sources. The 3.6–24 μm wavelength range measures the redshifted stellar flux peak and the beginning of the Rayleigh–Jeans tail, while dusty starbursts may in principle show enhanced 24 μm emission. This makes the survey particularly well suited to identify massive ellipticals and dusty starbursts. This paper presents first results from a pilot study of the quasar 3C 270.1 at $z = 1.53$, combining our *Spitzer* data with z'- and Y-band maps. Distances and ages in this paper are based on a lambda cold dark matter (ΛCDM) cosmology with $H_0 = 71$ km s^{-1} Mpc^{-1}, $\Omega_{\rm m} = 0.27$, and $\Omega_{\Lambda} = 0.73$.

2. OBSERVATIONS AND DATA

The *Spitzer* maps of 3C 270.1 were obtained using the instruments Infrared Array Camera (IRAC; 3.6–8.0 μm; Fazio et al. 2004) and Multiband Imaging Photometer for *Spitzer* (MIPS; 24 μm; Rieke et al. 2004). On-source exposure times were 4×30 s (each IRAC band) and 10×10 s (MIPS). The dithered maps (PID 40072; P.I.: G. Fazio) cover about 4′ field of view (FOV) with full depth. In addition, comparison fields offset 6′.5 from the main field were automatically obtained in the IRAC bands, at 3.6 μm and 5.8 μm northeast and at 4.5 μm and 8.0 μm southwest of the central field containing the quasar.

The maps allow us to detect sources down to ∼4 μJy (3σ) at 3.6 and 4.5 μm and 100 μJy at 24 μm.[6]

Complementary z'- and Y-band images were obtained at the 6.5 m MMT using MegaCam (30′ FOV; McLeod et al. 2006) and SWIRC (5′ FOV; Brown et al. 2008). The z'- and Y-bands (centered at 0.89 and 1.05 μm, respectively) bracket the 4000 Å break at redshift $z = 1.53$. Sensitivities better than 1 μJy were achieved at z' and Y band under good seeing conditions (FWHM <1″) with exposure times of 40 and 90 minutes, respectively. The z'-band image covers the IRAC comparison fields, but the Y image does not. At Galactic latitude $b = 80°.6$, foreground extinction is negligible ($E_{B-V} = 0.012$ mag).

The images were reduced using interactive analysis tools. The IRAC mosaics were corrected for the residual images that arise from prior observations of bright sources by making object-masked, median-stacked co-adds with all the science frames and then subtracting them from the science frames prior to final co-adding. Thus, we can be sure that there are no faint spurious signals in the IRAC mosaics arising from prior observations. For IRAC, we used the basic calibrated data products (BCD, version S16) and coadded them to 0″.869 pixels using version 4.1.2 of IRACProc (Schuster et al. 2006). This optimally handles the slightly undersampled IRAC PSF in order to assure accurate point-source photometry. For MIPS, we used custom routines to modify the version S17 BCD files to remove instrumental artifacts (e.g., residual images) before shifting and coadding to create the final mosaics. The MegaCam and SWIRC frames were reduced using standard procedures.[7]

The 3.6 μm image shows more sources than any other, and we used it as the source detection image for constructing a multiband catalog. In the central $4' \times 4'$ with optimal depth, 274 objects are detected at 3.6 μm, with 272/202/212 of them being also detected at 4.5/5.8/8.0 μm. At shorter wavelength, 184 (150) of the 3.6 μm sources are detected at z' (Y), and 143 at both z' and Y. The sources were extracted and matched using the SEXTRACTOR tool (Bertin & Arnouts 1996). Details are described in Appendix A. The photometric uncertainties are typically less than 10% but increase for the faintest sources.

The region of 3C 270.1 has also been mapped with the Sloan Digital Sky Survey (SDSS, DR6). About 35 relatively bright SDSS sources are identified with foreground galaxies and stars. These objects are excluded from the following discussion. In addition, we found an archival *Hubble Space Telescope* (*HST*) WFPC2 snapshot image of 3C 270.1 in the F702W pass band (600 s exposure time; P.I.: W. Sparks; Lehnert et al. 1999). Because of the limited spatial coverage and sensitivity (0.6 μJy), we did not use the F702W photometry for finding potential cluster members. However, the *HST* image enables us to inspect the morphology of a few of the sources to determine whether they are pointlike or extended and to look for rest-frame UV excesses.

3. RESULTS AND DISCUSSION

3.1. Cluster Galaxy Candidates

Cluster galaxies around 3C 270.1 should lie at the redshift of the quasar. We determined photometric redshifts z_{phot} by fitting

the observed spectral energy distributions (SEDs) of the 184 galaxies detected at z' with two basic templates, an elliptical galaxy and a dusty starburst galaxy.[8] For the elliptical galaxy, we used NGC 221, which has a strong 4000 Å break. The NGC 221 spectral template from Kinney et al. (1996), covering the rest-frame wavelength range 3000–8000 Å, was smoothly extrapolated to longer wavelengths by a 4000 K blackbody. For the starburst galaxy template, we used the ultraluminous infrared galaxy Arp 220 with photometry from the NASA Extragalactic Database (NED) and the SDSS (DR6) and mid-IR spectra from *Spitzer*/IRS. We also tested the dust-reddened star-forming galaxy template M 82, but the results were similar to those for Arp 220 (differences in z_{phot} less than $\Delta z = 0.1$), and therefore we present only the Arp 220 results.

The accuracy of photometric redshifts can be estimated, for instance, from the *Spitzer* Wide-Area Infrared Extragalactic Survey (SWIRE), which has spectroscopic redshifts available for many of its sources. In SWIRE, seven filters (five optical and two IRAC) were sufficient to discriminate between eight templates (ranging from blue to red galaxy types) and to determine z_{phot} with an rms of $\Delta z/(1 + z) = 3.5\%$ (Rowan-Robinson et al. 2008). We have fewer filters than SWIRE, but our task is easier because we only have to determine whether the photometry is consistent with $z = 1.53$ or not. Furthermore, we consider only extremely red sources and only two templates and therefore suggest that we can reach accuracy similar to that of SWIRE. At $z = 1.5$, an accuracy (rms) of about 4% corresponds to $\Delta z = 0.1$. This is much larger than the expected redshift dispersion within a cluster ($\Delta z < 0.01$). While the SEDs can provide cluster galaxy candidates within appropriate redshift bins around z_{QSO}, confirmation of a cluster will require spectroscopic redshifts of at least a sample of the candidates.

Figures 1 and 2 show examples of SEDs and template fits to cluster galaxy candidates. The most striking SED features are the steep rise from z' to Y band and beyond and the decline between 3.6 and 8.0 μm. The slopes of these features determine the redshift. We performed the template fits over a grid in redshift ($dz = 0.01$) and intensity. For a red SED with $F(3.6)/F(z') \approx 30$, the χ^2 contour plots exhibit a sharp minimum, suggesting that for a given template the achievable accuracy of z_{phot} is about $\Delta z = 0.1$. As illustrated in Figure 2, even for SEDs with fewer than six data points the accuracy of z_{phot} should be not worse than $\Delta z < 0.20$. Therefore, we have chosen as cluster galaxy candidates the 29 objects for which either the elliptical or the starburst template yields $1.33 < z_{phot} < 1.73$. The basic conclusions on the clustering of EROs around 3C270.1 remain unchanged for other ranges $|\Delta z|$ between 0.15 and 0.25.

Usually the 0.9–8.0 μm SEDs can be fitted very well with both the elliptical and the starburst template. Both templates are extremely red, and therefore no other galaxy type is likely to fit the SEDs. The examples in Figures 1 and 2 illustrate the ability to identify the two galaxy types at $z \sim 1.53$. The resulting fit parameters for the 29 cluster candidates are listed in Table 1. The photometric redshifts differ systematically for the elliptical and starburst templates. On average, z_{ell} is higher by 0.27 ± 0.1 than z_{SB}. Among the 29 cluster candidates, the elliptical template yields better fits (smaller χ^2 values) for 22 sources (75%; Table 1). All of these sources lie in the redshift bin $1.33 < z_{SB} < 1.73$. Among the remaining seven cluster

---

[6] We have also obtained a 16 μm map with the IRS peak-up array (4×14 s; Houck et al. 2004) which has been useful for the quasar SED (Haas et al. 2008). Because of the limited sensitivity (100 μJy) and small size (1′.5×2′), this map does not provide useful constraints for the cluster search. Therefore, the 16 μm data are not further considered here.

[7] See http://www.cfa.harvard.edu/∼mashby/megacam/megacam_frames.html for MegaCam.

[8] We also tried type-1/-2 active galactic nucleus (AGN) templates, but none of the SEDs are consistent with such templates at redshift $z \sim 1.5$ except 3C 270.1 itself.
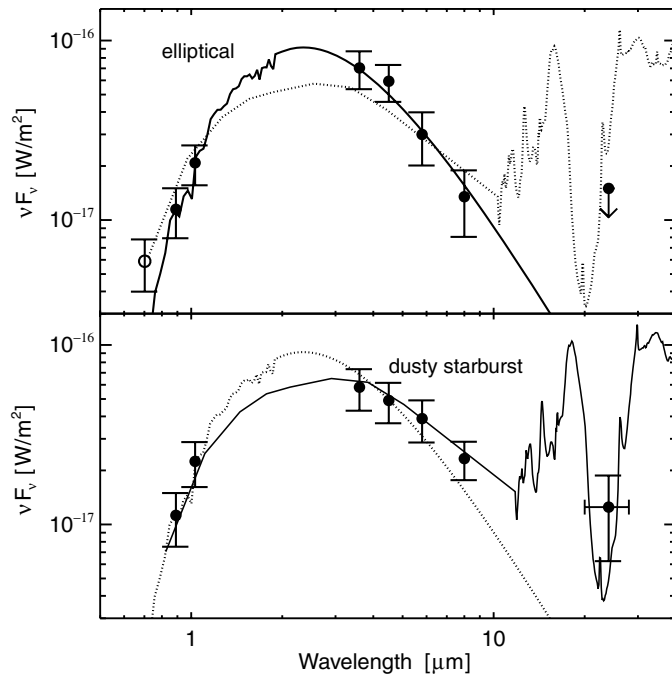
Figure 1. Observed SEDs for two good examples of the 29 cluster candidates. The IRAC and MMT data are marked with filled circles and 1σ error bars. The MIPS 24 μm data point is marked with a filled circle, too; in the upper panel (elliptical source) it is a 3σ upper limit, in the lower panel (dusty starburst source) it is a 2σ detection also visible on the map. The horizontal bar indicates the 24 μm pass band for comparison with the silicate absorption feature. *HST* photometry is marked with an open circle; it is not available for the dusty starburst source. The solid lines show the elliptical galaxy (NGC 221) fit for the source in the upper panel and the dusty starburst (Arp 220) fit for the galaxy in the lower panel. The dotted lines show the alternative template for each galaxy. The upper and lower panels show object numbers 23 and 3, respectively, as listed in Table 1.

Figure 2. Observed SEDs for two cluster candidates with poorer data quality. The IRAC and MMT data are marked with filled circles and 1σ error bars. The sources are detected only in the z'-band (in the lower panel also in the Y band) and at 3.6 and 4.5 μm, but the upper limits at 5.8 and 8.0 μm help to constrain the redshift fits. As in Figure 1, the upper panel shows a source (object 11) which is preferably fit by the elliptical template and the lower panel one (29) fit by the starburst template. The dotted and dashed lines show the preferred templates at different redshifts (indicated in the figure), showing that the accuracy of the photometric redshifts should be $dz \lesssim 0.2$.

candidates, those three sources which favor the starburst fit lie in the redshift bin $1.33 < z_{SB} < 1.73$, too. These sources have $\chi^2_{SB} < 0.3 \cdot \chi^2_{ell}$ (object numbers 3, 5, and 29 in Table 1). The remaining four sources (object numbers 11, 14, 17, and 28) are not detected at 5.8 and 8.0 μm, and they do not clearly favor the starburst template, so that—as ellipticals—they are cluster galaxy candidates.

The cluster galaxy candidates occupy a limited range of $z' - [3.6]$ color as shown in Figure 3. While the candidates were determined from multiband SED fitting (usually 4–6 bands), selecting a color range of $15 < F(3.6)/F(z') < 52$ would have given nearly the same sample. The sources redder than this color range are probably at larger redshift ($z > 1.8$), while bluer sources are consistent with being either foreground objects or unreddened star-forming galaxies at the quasar redshift. Our EROs with $F(3.6)/F(z') > 15$ (corresponding to $z' - [3.6] > 5$ mag in the Vega system) are likely to also obey the standard ERO definition of $R - K > 5$ mag (see Wilson et al. 2004).

3.2. Sky Distribution and Surface Density

Figure 4 shows the sky distribution of the cluster candidates. Spreading over a diameter of more than $2'$, they form at most a loose concentration around the quasar, indicating a protocluster rather than a virialized, concentrated system. The peak density appears to lie $\sim 30''$ to the east of 3C 270.1, but it is difficult to be precise with so few galaxies. The 3C 270.1 protocluster is larger in angular size than the X-ray clusters at $z = 1.45$ and $z = 1.22$ found by Mullis et al. (2005) and Bremer et al. (2006).
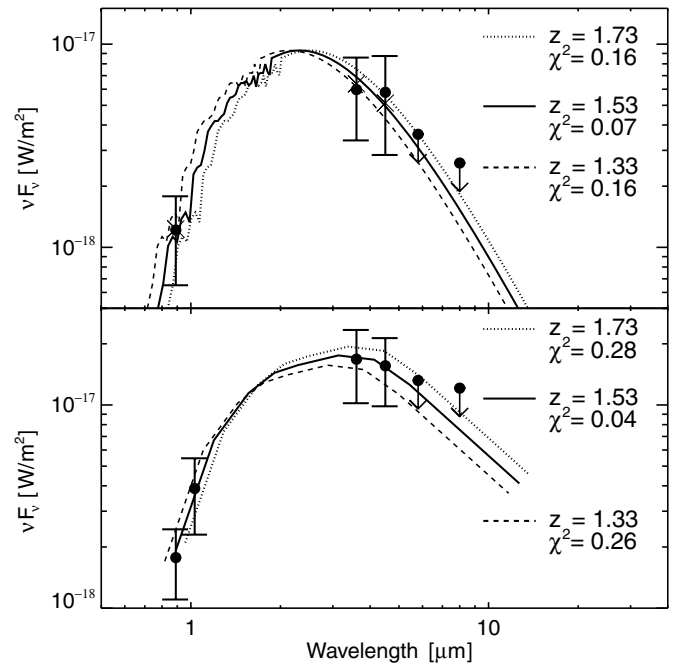
These clusters have an extent of less than $1'$ in both their galaxy distributions and their X-ray sizes.

We have also analyzed the two comparison fields taken with IRAC and covered by the MegaCam z' image (but not the SWIRC Y image). Details of the analysis are described in Appendix B. The surface density of possible $z = 1.53 \pm 0.20$ galaxies is less than about 18 objects in each control field of area 15.2 arcmin^2 (1.2 arcmin^{-2}). Thus, in the redshift range $z = 1.53 \pm 0.20$, the central field surrounding the quasar shows an excess of at least about $29 - 18 = 11$ sources, i.e., 60% over the comparison fields.

Figure 5 shows the radial surface density plot of the 29 EROs in the redshift range $z = 1.53 \pm 0.20$. The surface density peaks inside the central $50''$ radius and declines steadily with increasing distance down to the surface density of the control fields. This provides further evidence that there is an excess of $z_{phot} \approx 1.53$ galaxies near 3C 270.1. The radial overdensity is also present when using circles around the centroid east of the quasar position.

Existing X-ray data on 3C 270.1 are inconclusive about the presence of a cluster. The quasar itself is clearly detected as a point source in our 10 ks *Chandra* data (B. J. Wilkes et al. 2009, in preparation). Weak extended X-ray emission (less than $20''$) is also present, but most of the counts come from the position of the southern radio lobe or from between the northern radio lobe and the quasar. *ROSAT* data (19.3 ks, 1993 May) show a strong detection of 3C 270.1, but at *ROSAT* resolution not only is there no way to separate cluster gas emission from quasar emission, but the emission is also heavily blended with that of

Table 1
Fit Parameters for the 29 Cluster Galaxy Candidates in the Quasar Field

Object	R.A. J2000	Decl. J2000	n^a	z_{ell}^b	χ_{ell}^2	z_{SB}^c	χ_{SB}^2
1	12 20 27.90	33 43 11.5	3	1.47	0.43	1.16	0.53
2	12 20 28.72	33 41 51.9	6	1.50	0.06	1.20	0.22
3	12 20 29.20	33 42 10.5	6	1.55	0.51	1.35	0.15
4	12 20 30.06	33 43 18.1	6	1.47	0.19	1.00	0.85
5	12 20 30.66	33 44 50.0	4	1.90	0.17	1.60	0.03
6	12 20 30.73	33 44 39.4	6	1.53	0.12	1.24	0.35
7	12 20 31.18	33 43 14.1	6	1.63	0.04	1.47	0.31
8	12 20 32.49	33 43 20.3	5	1.50	0.29	1.34	0.39
9	12 20 33.50	33 42 25.4	5	1.35	0.10	1.11	0.38
10	12 20 33.57	33 44 08.3	4	1.42	0.13	1.16	0.18
11	12 20 33.85	33 45 37.5	3	1.53	0.07	1.22	0.03
12	12 20 33.90	33 42 34.6	4	1.36	0.08	1.17	0.30
13	12 20 34.79	33 41 55.4	5	1.47	0.10	1.07	0.27
14	12 20 34.95	33 42 41.0	4	1.45	0.01	1.20	0.01
15	12 20 35.20	33 42 09.6	5	1.35	0.12	0.96	0.43
16	12 20 35.88	33 43 32.2	4	1.59	0.07	1.28	0.10
17	12 20 36.50	33 43 30.6	4	1.40	0.19	1.20	0.10
18	12 20 37.70	33 41 18.2	5	1.54	0.34	1.33	0.37
19	12 20 38.52	33 43 04.2	4	1.53	0.05	1.25	0.08
20	12 20 38.78	33 43 50.2	6	1.68	0.32	1.38	0.53
21	12 20 39.16	33 44 31.9	4	1.50	0.01	1.27	0.03
22	12 20 40.10	33 43 20.5	6	1.50	0.23	1.36	0.35
23	12 20 40.49	33 43 21.9	6	1.56	0.13	1.04	0.98
24	12 20 40.55	33 43 17.3	4	1.63	0.03	1.55	0.06
25	12 20 40.62	33 43 00.2	4	1.48	0.01	1.25	0.02
26	12 20 43.31	33 42 51.2	5	1.50	0.44	1.32	0.66
27	12 20 43.32	33 44 19.8	5	1.69	0.01	1.37	0.04
28	12 20 44.17	33 44 03.9	4	1.56	0.11	1.27	0.07
29	12 20 45.13	33 43 18.9	4	1.84	0.26	1.53	0.04

Notes.
^{a} Number of data points (detections) used to calculate χ^2 of the fit.
^{b} Redshift of the fit using the elliptical template NGC 221.
^{c} Redshift of the fit using the starburst template Arp 220.

unrelated QSO B1223+338B located 0.''8 away.[9] We found no *XMM* observations. Longer *Chandra* exposures will be needed for a definitive detection of any X-ray emission from cluster gas.

3.3. Nature of Cluster Galaxy Candidates

The cluster galaxy candidates have an absolute rest-frame magnitude $H \approx K < -23.8$ (AB system). An $L^\star$ galaxy at $z \sim 1.5$ has $H \approx K = -23.6$ (as determined from observations at $1 < z < 1.3$ by De Propris et al. 2007). Thus only the most luminous cluster galaxy candidates are detected on our maps. The galaxies are either giant ellipticals or dust-reddened starbursts. If giant ellipticals, most of their stellar mass has been formed at even higher redshift, but they may harbor some ongoing star formation—it would be relatively weak with respect to the already existing stellar mass but could show up at rest UV wavelengths. If dusty starbursts, they would have to be at least three times more luminous in the near-infrared than the ULIRG Arp 220, indicating that a large stellar mass has already formed during an earlier episode.

The distinction between ellipticals and dusty starbursts is difficult to make at rest wavelengths shorter than 1 μm using photometry only, albeit possible with adequate wavelength coverage (Pozzetti & Mannucci 2000). At $z = 1.5$, the six
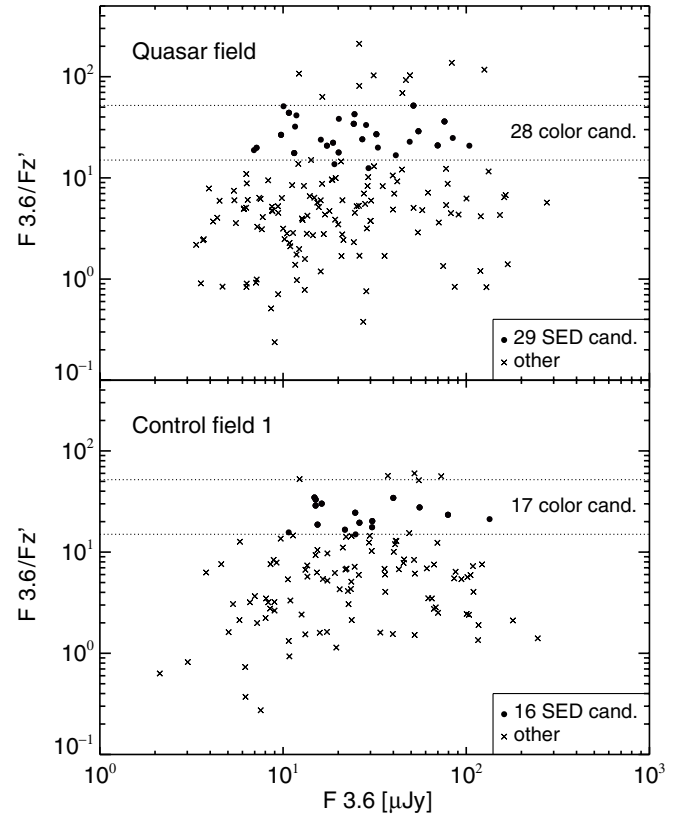
Figure 3. Color–magnitude diagram (CMD) $F(3.6)/F(z')$ vs. $F(3.6)$, for the quasar field (upper panel) and control field 1 (lower panel). Sources with $z_{phot} = 1.53 \pm 0.20$ (SED determined candidates marked with circles) concentrate in a distinct color range $15 < F(3.6)/F(z') < 52$ indicated by the horizontal dotted lines. The number of color-determined candidates is also given.
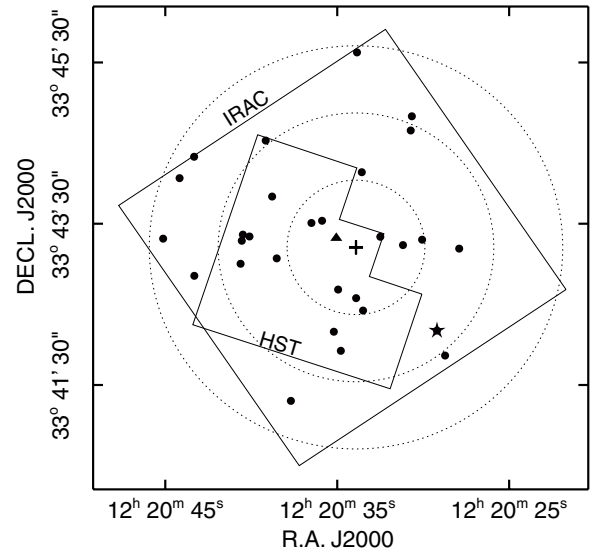

Figure 4. Sky distribution of the 29 candidate cluster galaxies around the quasar 3C 270.1 (marked with a cross). The triangle shows the apparent centroid of the cluster galaxy distribution. The star in the southwest marks the starburst candidate whose SED is shown in Figure 1. The solid lines surround the areas covered by IRAC and *HST* frames. The dotted circles of radius 50'', 100'', and 150'' outline the areas considered in Figure 5, they are centered around the quasar. At $z = 1.53$, 50'' corresponds to 427 comoving kpc.

data points of our SEDs cover about rest wavelength 0.3–3 μm. As mentioned in Section 3.1, 75% of the SEDs are better
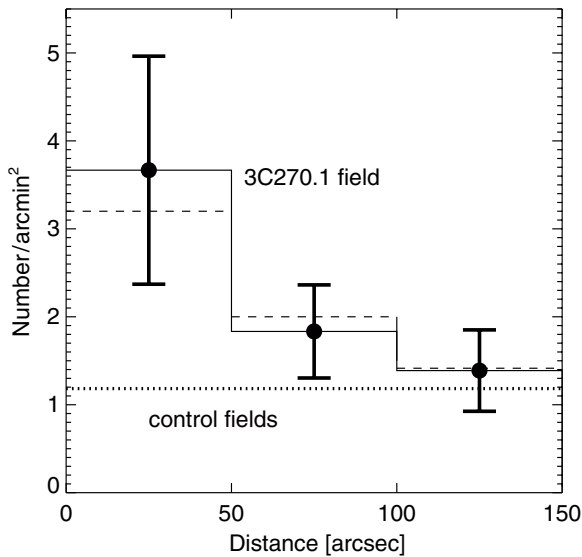
Figure 5. Surface density of the 29 cluster galaxy candidates vs. projected distance from the quasar 3C270.1 (solid line through fat dots with Poisson error bars). The radial bins centered around the quasar are outlined in Figure 4, and the surface density of the outermost annulus has been corrected for the area not covered by IRAC. For comparison, the long-dashed histogram shows the surface density of cluster galaxy candidates vs. the projected distance from centroid (the triangle in Figure 4). The dotted line indicates the mean surface density in the two control fields.

fitted by the elliptical than the starburst template. In principle, additional sensitive photometry at rest wavelengths longer than 10 μm could improve the starburst–elliptical distinction (Stern et al. 2006). At $z = 1.53$, unfortunately, the 9.7 μm silicate absorption enters the 24 μm band, reducing the potential to detect the powerful MIR emission of starbursts. Apart from 3C 270.1 itself, there is only one cluster candidate with a marginal (2σ) detection at 24 μm (Figure 2). Its SED provides evidence for a dust-enshrouded starburst. While only elongated on the Y-band image, on the z'-band image this galaxy appears as a double source with $0\rlap{.}''8$ (∼7 kpc) separation; for determining $z_{\rm phot}$ we have used the combined z'-band photometry. This source is not covered by the *HST* image (Figure 4).

Because the z'-band image is limited in spatial resolution, we have also inspected the morphology of the sources seen on the *HST* snapshot image. The *HST* frame covers 15 potential cluster galaxies (Figure 4), nine of which are detected. All nine are extended, ruling out the (remote) possibility that they might have been brown dwarfs. Figure 6 shows the four sources detected in the F702W filter with photometric accuracy better than 5σ. The SEDs of these galaxies are best fit with the elliptical template. They have a regular shape, and none of them show a peculiar morphology. This argues against starburst galaxy pairs and in favor of an evolved elliptical population. The remaining five of the nine *HST*-detected sources are too faint to draw stringent morphological conclusions.

The *HST* F702W photometry is of limited use because of the short exposure time, but six of the nine detected sources appear to show a rest-frame UV excess above the elliptical template (Figure 2). This indicates some level of ongoing star formation activity. However, at rest wavelengths around 1 μm this activity appears to be outshone by large numbers of already evolved stars.

Having as many as ∼11 galaxies brighter than $L^\star$ would be very high for a local cluster, but passive evolution will cause

these galaxies to become fainter by something like 3 mag[10] by $z = 0$ to become comparable to today's cluster ellipticals. Thus, the photometric data are compatible with the existence of a cluster.

4. CONCLUSIONS

High-redshift radio sources are predicted to serve as signposts for galaxy clusters in the early universe. In a pilot study using sensitive, large maps from the *SST* and the 6.5 m MMT, we find a clustering of red galaxies around the $z = 1.53$ quasar 3C 270.1.

1. Photometric redshifts identified 29 galaxies consistent with the quasar's redshift. While moderate clustering is evident in both the radial surface density of these objects and in their numbers with respect to nearby control fields, the sky distribution of the EROs suggests a loose, not-yet-virialized protocluster. Deep, high angular resolution X-ray observations are required to see whether hot intracluster gas is present or not.

2. The cluster-candidate galaxies have $z' - [3.6]$ colors indicative of EROs. They may be either dusty starbursts or elliptical galaxies with little ongoing star formation. The SED fits favor the majority of the potential cluster members being passive ellipticals, and this is consistent with the four objects with good *HST* images having undisturbed morphology. In some cases, the *HST* photometry reveals a rest-frame UV excess over the elliptical template, consistent with modest ongoing star formation and/or nuclear activity in these galaxies, but they must have formed the bulk of their stars at redshifts >1.53.

This pilot study demonstrates that the *Spitzer*/IRAC maps provide an efficient way to search for clustering of red galaxies around high-redshift radio sources, but accurate redshifts and the nature of the galaxies have to be confirmed with additional spectroscopy and/or deep far-infrared imaging with the *Herschel Space Observatory*. The ongoing investigation of all 64 high-redshift 3CR sources will result in a homogeneous database of considerable cosmological impact.

---

[10] Passive evolution was estimated via a Starburst99 model (Vázquez & Leitherer 2005) with an instantaneous burst age 1 Gyr before $z = 1.53$ and thus an age of 10 Gyr at $z = 0$.
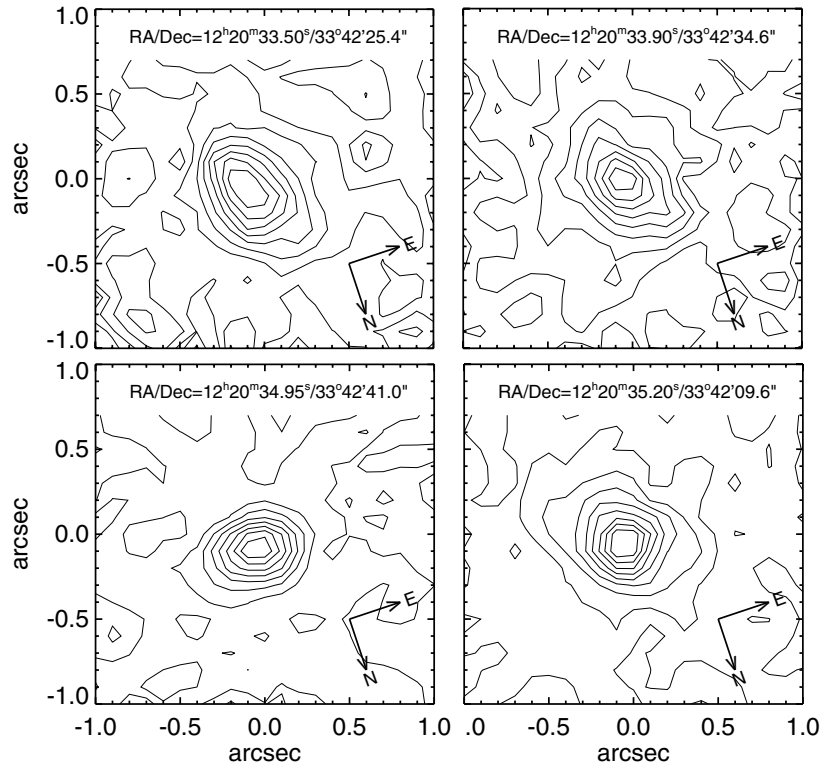
Figure 6. *HST* F702W images of the four cluster galaxy candidates (object numbers 9, 12, 14, and 15 in Table 1). The contours are linearly spaced in steps of 10% of the peak flux value (0%, 10%, . . . ,90%). The arrows indicate the orientation of each panel.

APPENDIX A

SOURCE EXTRACTION AND PHOTOMETRY

For source extraction and photometry, we used the SExtractor tool[11] (Bertin & Arnouts 1996, version 2.5). This tool is able to identify sources via a tree structure algorithm, provide their total magnitudes, and, if a saddle point is present in their profile, to deblend components via a multi-isophotal analysis. Photometry is derived using automatically adjusted apertures (option MAG-AUTO) following Kron's first moment algorithm (Kron 1980; Infante 1987). In case close neighbors are found, the components are iteratively deblended, with the photometric uncertainty of the faint companion reaching 25% in the worst cases (Beard et al. 1991).

In a first step, we adjusted the SExtractor parameters for each image (single-image mode). The parameters are, for instance, noise threshold and minimum number of connected pixels defining a source. The MMT z'- and Y-band images had a seeing of about $0\rlap{.}''9$ (FWHM), the IRAC PSF has FWHM between $1\rlap{.}''4$ at 3.6 μm and $1\rlap{.}''7$ at 8.0 μm. Typical Kron radii of the sources (containing 90% of the flux) are about 3–4$''$ in all filters (except 24 μm), so that the PSF differences play a minor role ($<5\%$), and the z'- and Y-band photometry—as computed by SExtractor—needs no aperture correction.[12] For the IRAC photometry, however, the absolute photometric calibration refers to an aperture of 12$''$, so we applied standard aperture corrections (5%–30%)[13] to derive the final photometry

of the sources, all of which are essentially unresolved. The very few sources detected at 24 μm are well separated, so that clean photometry could be derived without need for aperture correction.

In a second step, we ran SExtractor in double-image mode on the 4.5, 5.8, and 8.0 μm IRAC maps, using as primary the 3.6 μm map because it contains more sources than any other IRAC map. The double-image mode is able to identify, for instance, for a 3.6 μm detection also the corresponding 4.5 μm source, even if it was not detected in single-image mode. The double-image mode enabled us to detect essentially all 3.6 μm sources at 4.5 μm (272 of 274 sources). The detection rate at 5.8 and 8.0 μm was lower (202 and 212 sources, respectively). We determined the 5.8 and 8.0 μm upper flux limits (≈ 7 μJy) from the break of the flux histograms of the detections. In case of non-detections and clean regions we used this flux value as the 3σ upper limit.

SExtractor was run separately on the z' image, and the z' and IRAC source lists were matched with a search radius of 1.5$''$. This should produce good identifications because no two IRAC sources are closer together than 3$''$. To check further how far confusion plays a role, we counted the number of MMT sources within a radius of 3$''$ around each IRAC source. By far most sources ($>90\%$) are unambiguously matched to a single z' source. Of 274 IRAC sources in the quasar field, 18 (6.6%) have two z' counterpart, and one even has three. The control fields show about the same statistics: nine double z' counterparts (4.4%) out of 205 IRAC sources in the 3.6 μm field and 10 double counterparts (6.0%) out of 167 IRAC sources in the 4.5 μm field. Thus, the fraction of confused sources is small and comparable for control and quasar fields, and therefore we do not expect that the clustering results are significantly affected by confusion. To avoid any possible complication, we have omitted from the analysis all sources (4%–7%) with two or

---

[11] http://terapix.iap.fr/IMG/pdf/sextractor.pdf
[12] Our MMT z'-band photometry was calibrated with the z-band image of the Sloan Digital Sky Survey (SDSS, DR6), including a (very small) color term to account for the similar but nonetheless different band passes. Our Y-band photometry was calibrated with interpolated total magnitudes from SDSS and Two Micron All Sky Survey (2MASS).
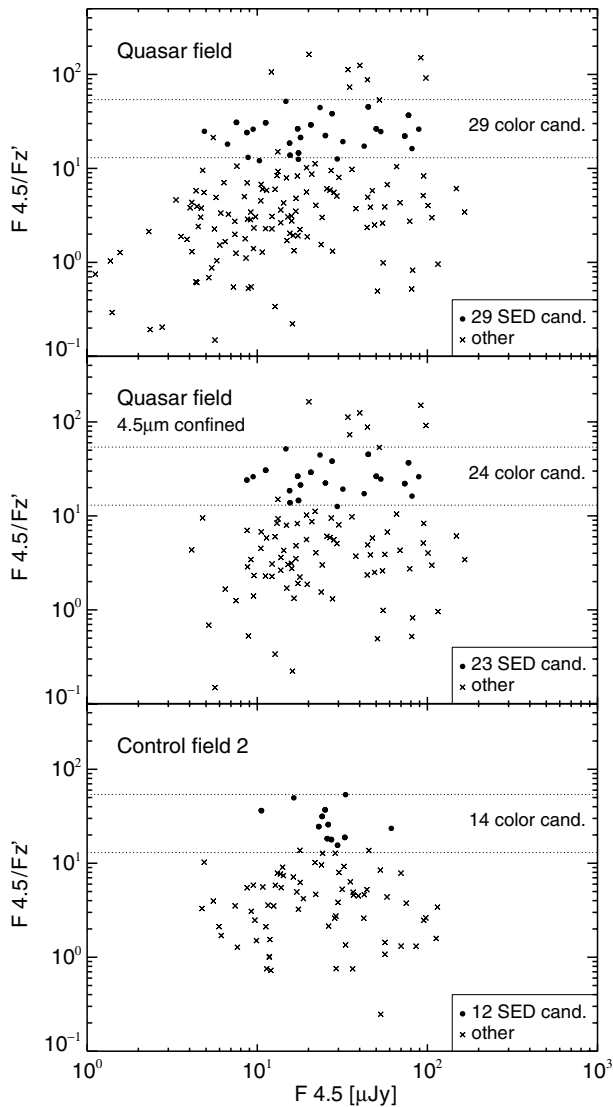[13] http://ssc.spitzer.caltech.edu/irac/dh/

Figure 7. CMD $F(4.5)/F(z')$ vs. $F(4.5)$ of the quasar field and control field 2. Top: quasar field with all sources detected at 4.5 μm using SExtractor in the double-image mode at 3.6 and 4.5 μm. Middle: quasar field restricted to those sources detected at 4.5 μm using SExtractor in the single-image mode, as was done for the control field 2. Bottom: control field 2. Sources with $z_{phot} = 1.53 \pm 0.20$ (SED-determined candidates marked with circles) concentrate in a distinct color range $13 < F(4.5)/F(z') < 54$ indicated by the horizontal dotted lines. The number of color-determined candidates is also given.

more z' counterparts found by SExtractor. The starburst cluster candidate galaxy (object number 3 in Table 1) remained in the sample because SExtractor treated it as a single source. Most likely the saddle between the two components is not deep enough for SExtractor to split them despite the source's visual appearance on the z' image as a 0''.8 double.

APPENDIX B

COMPARISON WITH THE CONTROL FIELDS

The quasar field has photometry in six filters, two MMT, and four IRAC bands. But the two control fields have photometry in only three filters, in z' and two IRAC bands: 3.6 and 5.8 μm in control field 1, 4.5 and 8.0 μm in control field 2. This makes the uncertainties on the photometric redshifts larger, and therefore comparison within the same redshift bin appears not to be

straightforward. Furthermore, in the central field, the source detection rate at 4.5 μm is lower than at 3.6 μm, so that for a fair comparison the number of candidates in control field 2 has to be corrected for. In order to facilitate the comparison, we used the colors $z' - [3.6]$ and $z' - [4.5]$ and counted the number of candidates in the respective color bins.

Control field 1. The colors of the elliptical and starburst template, when redshifted to $z = 1.53$, are $F(3.6)/F(z') = 25$ and 39, respectively. In the color range $15 < F(3.6)/F(z') < 52$ we found 28 and 17 sources for the quasar and the control field, respectively (Figure 3). With regard to the low number statistics, these values are consistent with the 29 and 16 sources in the quasar and the control field, having $1.33 < z_{phot} < 1.73$ (denoted as SED candidates in Figure 3). This leaves an excess of 11 color- and 13 SED-selected sources in the quasar field.

Control field 2. The colors of the elliptical and starburst template, redshifted to $z = 1.53$, are $F(4.5)/F(z') = 24$ and 43, respectively. Guided by these "expectation values" and the actual $z' - [4.5]$ distribution of the candidates in the quasar field, we selected a color range of $13 < F(4.5)/F(z') < 54$ (Figure 7, top). Now we considered the fields, where the 4.5 μm source list was created using the single-mode SExtractor option, i.e., not making use of the 3.6 μm information in the quasar field. We found 24 and 14 color-selected candidates for the quasar and the control field, respectively (Figure 7, middle and bottom). These values are consistent with the corresponding numbers for SED-selected candidates of 23 and 12 in the quasar and the control field, respectively. Because the quasar field contains more cluster galaxy candidates, 29 via color and 29 via z_{phot} (Figure 7, top), we have scaled up the number of candidates in the control field by the factors 29/24 for the color candidates and 29/23 for the SED candidates. This results in 17 color- and 15 SED-selected candidates. This leaves an excess of 12 ($= 29 - 17$) color- and 14 ($= 29 - 15$) SED-selected sources in the quasar field.

Combining the control field counts we estimate an excess of 11–12 color- and 13–14 SED-selected candidate cluster galaxies in the quasar field.

REFERENCES

Beard, S. M., McGillivray, H. T., & Thanisch, P. F. 1991, MNRAS, 247, 311
Bertin, E., & Arnouts, S. 1996, A&AS, 117, 393
Best, P. 2000, MNRAS, 317, 720
Bremer, M. N., et al. 2006, MNRAS, 371, 1427
Brown, W., McLeod, B. A., Geary, J. C., & Bowsher, E. C. 2008, Proc. SPIE, 7014, 90
De Propris, R., Stanford, S. A., Eisenhardt, P. R., Holden, B. P., & Rosati, P. 2007, AJ, 133, 2209
Eisenhardt, P. R., et al. 2008, ApJ, 684, 905
Fang, T., et al. 2007, ApJ, 660, L27
Fazio, G. G., et al. 2004, ApJS., 154, 10
Haas, M., et al. 2008, ApJ, 688, 122
Houck, J. R., et al. 2004, ApJS, 154, 18
Infante, L. 1987, A&A, 183, 177
Intema, H. T., et al. 2006, A&A, 456, 433
Kinney, A., et al. 1996, ApJ, 467, 38
Kron, R. G. 1980, ApJS, 43, 305
Kurk, J. D., et al. 2000, A&A, 358, L1
Lehnert, M. D., Heckman, T. M, & Weaver, K. A. 1999, ApJS, 123, 351
McLeod, B., Geary, J., Ordway, M., Amato, S., Conroy, M., & Gauron, T. 2006, in Scientific Detectors for Astronomy 2005, ed. J. E. Beletic, J. W. Beletic, & P. Amico (Berlin: Springer), 337
Miley, G., et al. 2004, Nature, 427, 47
Mullis, C. R., et al. 2005, ApJ, 623, L85
Muzzin, A., Wilson, G., Lacy, M., Yee, H. K. C., & Stanford, S. A. 2008, ApJ, 686, 966
Pozzetti, L., & Mannucci, F. 2000, MNRAS, 317, L17

Rieke, G. H., et al. 2004, ApJS, 154, 50
Rowan-Robinson, M., et al. 2008, MNRAS, 386, 697
Sánchez, S. F., & González-Serrano, J. I. 2002, A&A, 396, 773
Schuster, M. T., Marengo, M., & Patten, B. M. 2006, Proc. SPIE, 6270, 65
Seymour, N., et al. 2007, ApJS, 171, 353
Stanford, S. A., et al. 2005, ApJ, 634, L129
Stanford, S. A., et al. 2006, ApJ, 646, L13
Stern, D., Holden, B., Stanford, S. A., & Spinrad, H. 2003, AJ, 125, 2759
Stern, D., et al. 2006, AJ, 132, 1405

Toft, S., Pedersen, K., Ebeling, H., & Hjorth, J. 2003, MNRAS, 341, L55
van Breukelen, C., et al. 2006, MNRAS, 373, L26
Vázquez, G. A., & Leitherer, C. 2005, ApJ, 621, 695
Venemans, B. P., et al. 2007, A&A, 461, 823
Werner, M. W., et al. 2004, ApJS, 154, 1
Wilson, G., et al. 2004, ApJS, 154, 107
Wold, M., et al. 2003, AJ, 126, 1776
Zatloukal, M., et al. 2007, A&A, 474, L5
Zirm, A. W., et al. 2008, ApJ, 680, 224